Passive Dynamics of High Frequency Bat Wing Flapping with an Anisotropic Membrane

Michael Zheng, S.M.Hadi Sadati*, Pendar Ghalamchi and Thrishantha Nanayakkara
Center for Robotics Research (CoRe), Department of Informatics
King's College London
London, United Kingdom
Seyedmohammadhadi.sadati@kcl.ac.uk

***Abstract*—We investigate how unmanned aerial vehicles (UAVs) with flexible wings can be designed to exploit the aeroelasticity of wing deformation that is present in bat wings, with a view to improve the efficiency of flight. We constructed a robotic bat wing with fully passive elastic wing-folding properties. The robotic wing is powered by a gearbox running two synchronised motors, effectively providing one degree of motion: the upstroke and down-stroke of the wing. Through numerical simulations and setup experiments, we observed that by integrating a span-wise elastic network into the bat wing, we were able to achieve passive wing-folding that mimics the 8-shape wing-folding seen in bats' high speed flight. This way, we were able to reduce the complexity and additional actuation associated with wing-folding in a robotic wing.**

Keywords—Bat; Flapping; Passive; Anisotropic Membrane; Simulation; Experiment

I. INTRODUCTION

The bat wing has an anisotropic stiffness distribution of elasticity. It exhibits high stiffness strength along the digits, compared to high failure strain in the perpendicular direction [1]. This distribution not only prevents high shear forces from developing between the bones and the wing membrane, but also helps to store energy by extending the membrane during the down-stroke. It is interesting to note that exploitation of passive dynamics arising from special distributions of body stiffness is seen not only in flapping flight, but also in other forms of locomotion such as swimming [2]. In [2], it has been demonstrated that a dead trout can passively start to swim against a stream of water by generating productive vortexes purely based on passive resonance of constructive body movements in hydraulic turbulence behind a cylindrical obstacle placed in the path of a water stream. These biological examples suggest that the management of the distribution of body elasticity plays a vital role in efficient locomotion. This opens the scientific question as to how the morphology of a deformable winged UAV should be designed to be able to tune to the flight environment without off-line planning.

By mimicking the properties of the bat wing, we may be able to increase the efficiency of airborne vehicles, an exciting prospect from an engineering perspective. Recently, advancements in engineering materials, actuators and controls have allowed us to consider mimicking flight behaviour in the natural world [3]. There has been analysis on a resonant drive to reduce the average battery power consumption for DC motor-driven flapping wing robots [4]. They developed a methodology using a non-dimensional analysis of a motor driven compliant system. Using this, they were able to guide the mechanical design and predict the optimal operating point based on power efficiency. A prototype of a biologically inspired UAV imitating the hovering flight of humming birds and dragonflies shows great potential in developing a high performance flapping micro-UAV [5]. There have been previous attempts to develop a bat inspired UAV, such as BATMAV [6], RoboBat [7], and recently in [8][9]. Here the authors aim to develop flexible wings actuated by artificial muscles, rather than exploiting the aero-elastic properties of the bat wing to improve the efficiency of flight; while similar research on insect size flyers showed advantages of anisotropic membrane in MAV's flight performance and control [10].

When considering the application of flapping flight, it is advantageous to reduce the weight of the ornithopter as much as possible. We seek to eliminate the need for active actuation of wing folding during flight which reduces the energetic cost on the upstroke of flapping flight [11]. Therefore, we look to the aeroelasticity of the bat wing membrane as inspiration to construct a passive wing folding technique that utilises the elasticity of the wing.

Flyers' flapping kinematics are different depending on the wing structure and flight speed [10][12] for which the aeroelasticity mechanisms should be investigated individually. Researchers at Brown University have developed a 3D printed articulated bat wing skeleton with a silicon membrane [13]. This study in particular highlights the advantages of wing folding, not only on energy conservation, but also in altering the aerodynamic qualities of the wing. Our aim is to build upon this foundation by focusing on the aeroelasticity of the bat wing as major factor in efficient high speed flight, in particular, how we can derive inspiration into wing-folding kinematics of high frequency flapping.Different species of bats have different properties [1]. Our aim is not to mimic the flight of bats, or one particular species. Rather we seek a solution with feasible applications in robotics and biomimetic, as well as the potential for further study. Here, we investigated the passive role of anisotropic wing membrane stiffness in reducing the complexity of the flapping motion.

978-1-4799-4598-6/14/$31.00

II. MODELLING

A. Kinematics

Fig. 1 shows our 3D bat wing model with three links (arm, forearm and hand) and four degrees of freedom (DOF). The shoulder joint is attached to the base frame origin. Base frame has an inclination equals to the wing geometrical angle of attack (AoA) (α_a) with gravity direction (g). The wing is approximated by a trapezoid with variable span but parallel root (c_r) and tip chords (c_t). The membrane is modelled a series of linear springs as the elastic elements along local chord-wise sweep directions. The model parameters are derived using a bat wing design [13] using Solidworks 2013. The shoulder rotation about the base frame x-axis (q_1) assumes a cosinusoidal form as in (1) and other three joints are not actuated actively and their axes of rotation are the local frames z-axis (q_2, q_3, q_4). The centre of mass (COM) for each link is centred at its midpoint. For simplicity and based on observation of a real bat flapping, the following constraints are being used between angles to reduce the under actuated order of the model to one.

$$c(q) = \begin{bmatrix} q_1 - \mathrm{A}.\cos(\omega.t + \pi) + q_{1_0} \\ q_3 - 2 \times q_2 \\ q_4 + 20° - 2 \times q_3 \end{bmatrix} = 0 \qquad (1)$$

Linear and angular velocity vectors of each element derived using 3×3 rotation ($R(q_i)$) and 4×4 transformation matrices ($TR(R,r_f)$) as in (2) where q_i is the angle of rotation, r_f is the row offset vector between two consecutive joint, rc is the COM absolute position vector (w.r.t. base frame) represented in base frame and $\boldsymbol{\omega}$ is the absolute angular velocity vector represented in local frame (attached to each link at its first joint with the link along its y axis and the first joint rotates along its z axis) for each link. a, f and h are subscripts for frames attached to, and the properties of the arm, forearm and hand links respectively. l_i is the link length.

$$R_{\mathrm{x}}(q_i) = \begin{bmatrix} 1 & 0 & 0 \\ 0 & \cos(q_i) & -\sin(q_i) \\ 0 & \sin(q_i) & \cos(q_i) \end{bmatrix}$$

$$R_{\mathrm{z}}(q_i) = \begin{bmatrix} \cos(q_i) & -\sin(q_i) & 0 \\ \sin(q_i) & \cos(q_i) & 0 \\ 0 & 0 & 1 \end{bmatrix}$$

$$TR(R, r_{\mathrm{f}}) = \begin{bmatrix} R & r_{\mathrm{f}}^{\mathrm{T}} \\ 0_{1\times3} & 1 \end{bmatrix}_{4\times4}$$

$$\boldsymbol{\omega}_{\mathrm{a}} = R_{\mathrm{z}}(q_2)^{-1}.[\dot{q}_1 \quad 0 \quad 0]^{\mathrm{T}} + [0 \quad 0 \quad \dot{q}_2]^{\mathrm{T}}$$

$$\boldsymbol{\omega}_{\mathrm{f}} = R_{\mathrm{z}}(q_3)^{-1}.\boldsymbol{\omega}_{\mathrm{a}} + [0 \quad 0 \quad \dot{q}_3]^{\mathrm{T}}$$

$$\boldsymbol{\omega}_{\mathrm{h}} = R_{\mathrm{z}}(q_4)^{-1}.\boldsymbol{\omega}_{\mathrm{f}} + [0 \quad 0 \quad \dot{q}_4]^{\mathrm{T}}$$

$$TR_{\mathrm{a}} = TR(R_{\mathrm{x}}(q_1).R_{\mathrm{z}}(q_2), [0 \quad 0 \quad 0])$$

$$TR_{\mathrm{f}} = TR(R_{\mathrm{z}}(q_3), [0 \quad l_{\mathrm{a}} \quad 0])$$

$$TR_{\mathrm{h}} = TR(R_{\mathrm{z}}(q_4), [0 \quad l_{\mathrm{f}} \quad 0])$$

$$rc_{\mathrm{a}} = TR_{\mathrm{a}}.[0 \quad l_{\mathrm{a}}/2 \quad 0]^{\mathrm{T}}$$

$$rc_{\mathrm{f}} = TR_{\mathrm{a}}.TR_{\mathrm{f}}.[0 \quad l_{\mathrm{f}}/2 \quad 0]^{\mathrm{T}}$$

$$rc_{\mathrm{h}} = TR_{\mathrm{a}}.TR_{\mathrm{f}}.TR_{\mathrm{h}}.[0 \quad l_{\mathrm{h}}/2 \quad 0]^{\mathrm{T}} \qquad (2)$$

B. Dynamics

We use a matrix representation for the equation of motion (EOM) in (3) using the TMT method in (4) to derive the dynamic model because of simplicity and efficient numerical evaluation as in [14]. q= $[q_1, q_2, q_3, q_4]$ is the generalised coordinates vector, M is the inertial matrix in the Lagrange equation, T_{cn} is the constrains Jacobian matrix on the generalised coordinates, λ is the Lagrange multipliers vector, d_{EOM} is the vector of the other terms in the Lagrange equation, and d_λ is the vector of the other terms in the constraint equations vector ($c(q)$) derivatives. $c(q)$ is differentiated multiple times, so its order of differentiation equals that of the EOM, namely two (6).

$$\begin{bmatrix} \bar{M} & T_{\mathrm{cn}}^{\mathrm{T}} \\ T_{\mathrm{cn}} & 0 \end{bmatrix} + \begin{bmatrix} \ddot{q} \\ -\lambda \end{bmatrix} = \begin{bmatrix} d_{\mathrm{EOM}} \\ d_\lambda \end{bmatrix} \qquad (3)$$

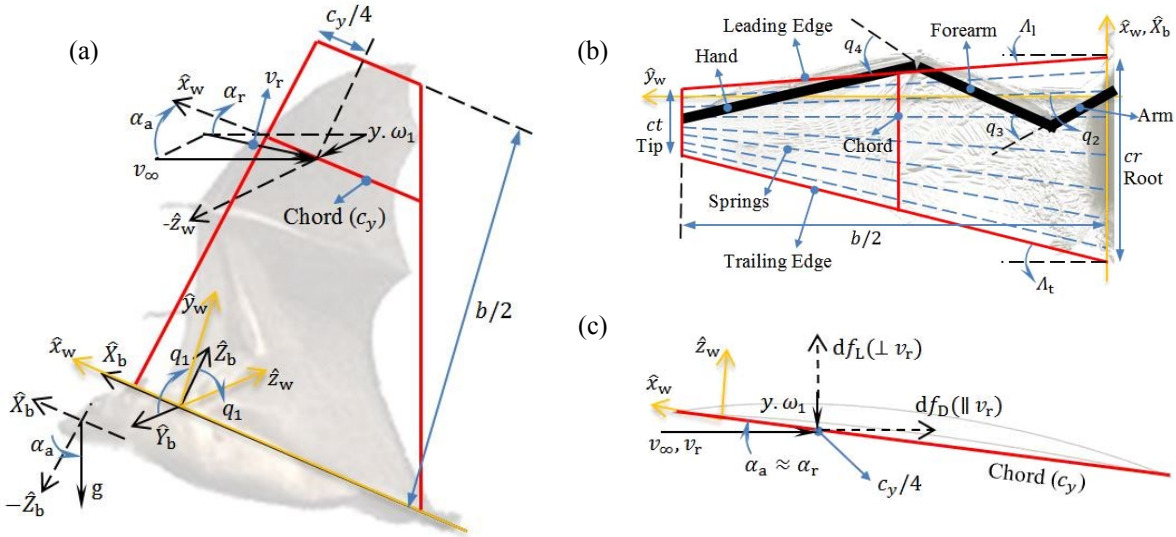

Fig. 1. Schematic model of a bat model: (a) base and wing frames, and apparent air stream due to free air stream and wing flapping motion at quarter chord of each element; (b) wing shematic with span-wise elastic elements; (c) aerodynamic forces on each element. b is the subscripts for the base frame and w is for the one attached to the wing surface whose origins are at the shoulder joint. Geometrical and real AoA are showed in left figure while they are approximated to be equal at the right-down figure.

Here T is the Jacobian matrix of x_{COM} which is the combination of links COM position (rc) and pseudo-rotation ($\int \boldsymbol{\omega}.\mathrm{d}q$) 3×1 vectors in terms of the generalised coordinates, m_i is i^{th} link mass, I_i is the i^{th} link 3×3 inertia matrix, f_g is the vector of conservative forces acting on each element such as gravity, and Q_c and Q_{nc} are the virtual work vectors of other conservative (here Q_k accounts for membrane elasticity (k) effect) and non-conservative forces (here Q_{damp} accounts for joints' rotational viscous damping (c_v) and Q_{aero} for aerodynamic forces (lift (f_L) and drag (f_D) effect) in generalized coordinate space [14].

$$
\begin{gathered}
x_{\mathrm{COM}\,[18\times1]} = [rc_{\mathrm{a}} \quad rc_{\mathrm{f}} \quad rc_{\mathrm{h}} \quad \int \boldsymbol{\omega}_{\mathrm{a}} \quad \int \boldsymbol{\omega}_{\mathrm{f}} \quad \int \boldsymbol{\omega}_{\mathrm{h}}]^{\mathrm{T}} \\
T_{[18\times4]} = \partial x_{\mathrm{COM}}(q)/\partial q \\
d_{[18\times1]} = -(\partial(T.\dot{q})/\partial q).\dot{q} \\
M_{[18\times18]} = \mathrm{diag}[m_i, m_i, m_i, I_{i[3\times3]}, \dots], (i: \mathrm{a, f, h}) \\
f_{\mathrm{g}} = -\mathrm{g}.[m_i.\sin(\alpha_{\mathrm{a}}), 0, m_i.\cos(\alpha_{\mathrm{a}}), 0,0,0, \dots]_{1\times18}{}^{\mathrm{T}}, (i: \mathrm{a, f, h}) \\
Q_{\mathrm{nc}} = Q_{\mathrm{damp}} + Q_{\mathrm{aero}}, \qquad Q_{\mathrm{c}} = Q_{\mathrm{k}} \\
Q_{\mathrm{damp}} = -\mathrm{c_v}.\dot{q}_{4\times1} \\
\bar{M} = T^{\mathrm{T}} M\, T^{\mathrm{T}} \\
d_{\mathrm{EOM}} = T^{\mathrm{T}}[f - M.d] + Q_{\mathrm{c}} + Q_{\mathrm{nc}}
\end{gathered} \tag{4}
$$

There is no need to find pseudo-rotation vectors. Here since we have ($v_b = T.\dot{q}$) as the combination of links' absolute linear and angular velocity vectors (v_b), we simply rearrange the absolute angular velocity vectors in (2), in the form of ($\boldsymbol{\omega} = T_{\boldsymbol{\omega}}.\dot{q}$) and then place the 3×4 coefficient matrices (T_ω) at their right place in T which is a 18×4 matrix (elements in the 9-18th rows).

T_{cn} is derived based on the three constraints in (1).

$$
\begin{gathered}
\ddot{c}(q) = T_{\mathrm{cn}}\ddot{q} + d_\lambda \\
T_{\mathrm{cn}} = \frac{\partial c(q)}{\partial q} = \begin{bmatrix} 1 & 0 & 0 & 0 \\ 0 & -2 & 1 & 0 \\ 0 & 0 & -2 & 1 \end{bmatrix} \\
d_\lambda = -[A\omega^2 \cos(\omega t + \pi) \quad 0 \quad 0]^{\mathrm{T}}
\end{gathered} \tag{5}
$$

C. Membrane Model

Membrane is modelled as a trapezoid by integrating span-wise elastic network of linear springs with elastic coefficient k and initial length l_0 as in Fig. 1. Membrane is rigid in chord-wise direction and does not have lateral deflection normal to the wing surface. Q_c=Q_k can be found from integrating springs' virtual work by having each ones deflection (l_k-l_0), direction (r_k) and attachment position to the wing tip (rt_k) as in (6). Here r_{tw} is hand tip position vector in wing frame, b is wing span, l_k is springs instantaneous length, η is chord length ratio, x_{lr} and x_{lt} are leading edge root and tip offset position from shoulder joint and hand tip along x-axis respectively, Λ_l, Λ_t and Λ_x are sweep angle at leading edge, trailing edge and any arbitrary position along x-axis, and f_k is each spring's force vector. We use $\cos(\Lambda_x)\approx1$ and $\tan(\Lambda_x)\approx\sin(\Lambda_x)\approx\Lambda_x$ approximations to reduce the complexity of integration.

$$
\begin{gathered}
r_{\mathrm{t_w}} = TR(R_{\mathrm{z}}(q_2), [0 \quad 0 \quad 0]).TR_{\mathrm{f}}.TR_{\mathrm{h}}.[0 \quad l_{\mathrm{h}} \quad 0]^{\mathrm{T}} \\
b = 2.r_{\mathrm{tw}_y}, \qquad l_{\mathrm{k}} \approx b/2 \\
\eta = c_{\mathrm{t}}/c_{\mathrm{r}} \\
\Lambda_{\mathrm{l}} \approx -2.(x_{\mathrm{lr}} - (r_{\mathrm{tw_x}} + x_{\mathrm{lt}}))/b \\
\Lambda_{\mathrm{t}} \approx -2.((c_{\mathrm{r}} - x_{\mathrm{lr}}) + r_{\mathrm{tw_x}} - (c_{\mathrm{t}} - x_{\mathrm{lt}}))/b \\
\Lambda_{\mathrm{x}} = \begin{cases} \Lambda_{\mathrm{l}}.(x - r_{\mathrm{tw_x}})/(x_{\mathrm{lr}} - r_{\mathrm{tw_x}}), & x \geq r_{\mathrm{tw_x}} \\ \Lambda_{\mathrm{t}}.(x - r_{\mathrm{tw_x}})/((c_{\mathrm{r}} - x_{\mathrm{lr}}) - r_{\mathrm{tw_x}}), & x < r_{\mathrm{tw_x}} \end{cases} \\
f_{\mathrm{k}} = -R_{\mathrm{x}}(q_1).[\Lambda_{\mathrm{x}} \quad 1 \quad 0]^{\mathrm{T}} \\
rt_{\mathrm{k}} = R_{\mathrm{x}}(q_1).[r_{\mathrm{tw_x}} - (c_{\mathrm{t}} - x_{\mathrm{lt}}) + \eta.(x - (c_{\mathrm{r}} - x_{\mathrm{lr}})) \quad b/2 \quad 0]^{\mathrm{T}} \\
Q_{\mathrm{k}[4\times1]} = \int_{-(c_{\mathrm{r}} - x_{\mathrm{lr}})}^{x_{\mathrm{lr}}} k.(l_{\mathrm{k}} - l_0).(\partial(rt_{\mathrm{k}}(q))/\partial q)^{\mathrm{T}}.f_{\mathrm{k}}.\mathrm{d}x
\end{gathered} \tag{6}
$$

D. Aerodynamic Model

Bat wing is approximated as a trapezoidal thin airfoil whose aerodynamic properties addressed in common aerodynamic handbooks widely using blade element theory and quasi-steady method [15]. Due to flapping motion, local effective AoA (α_r) along wing span alters as the magnitude of normal velocity of the wing element increases. For simplicity effective and geometrical AoA (α_a) are considered equal and $\cos(\alpha_r)\approx1$ and $\sin(\alpha_r)\approx\alpha_r$ which is feasible for low AoA, high speed flapping and forward flight, however the change in local air stream along the wing span is considered. Aerodynamic forces are exerted on quarter-chord from leading edge at each element. Total normal (f_{nw}) and tangential (f_{tw}) aerodynamic forces are derived based on drag (C_D) and lift coefficients (C_L) of a finite 3-D trapezoidal wing as in [15] to find the vector of centre of pressure (CoP) (rp_w), where the instantaneous total force can be considered to be exerted, all in the wing frame. Here AR is the wing aspect ratio, c_y is element chord length, $\Lambda_{0.25}$ is the local quarter-chord sweep angle, a_0 and a are lift curve slope for 2-D infinite and 3-D finite thin airfoil, e_w is the Oswalt (span) efficiency factor, $\mathrm{d}f_L$ and $\mathrm{d}f_D$ are each element drag and lift force magnitudes, ρ is the air density, and m_x and m_y are momentum of aerodynamic forces about wing frame x and y axes.

$$
\begin{gathered}
\alpha_{\mathrm{r}} \approx \alpha_{\mathrm{a}}, \qquad AR = 2.b/(c_{\mathrm{r}}.(1+\eta)) \\
c_{\mathrm{y}} = c_{\mathrm{r}}.(1 - 2.y.(1-\eta)/b) \\
\tan(\Lambda_{0.25}) = \tan(\Lambda_{\mathrm{l}}) - (1-\eta)/(AR.(1+\eta)) \\
a = \pi.AR/(1 + \sqrt{1 + (\pi.AR/(a_0.\cos(\Lambda_{0.25})))^2}), \\
a_0 = \pi \\
\mathrm{C_L} = a.\alpha_{\mathrm{r}}, \qquad \mathrm{C_D} = \mathrm{C_{D_0}} + \mathrm{C_L^2}/(\pi.AR.\mathrm{e_w}) \\
\mathrm{d}f_{\mathrm{L}} = \rho.\mathrm{C_L}.(y^2.\dot{q}_1^4 + v_\infty^2).c_{\mathrm{y}}.\mathrm{d}y/2 \\
\mathrm{d}f_{\mathrm{D}} = \rho.\mathrm{C_D}.(y^2.\dot{q}_1^4 + v_\infty^2).c_{\mathrm{y}}.\mathrm{d}y/2 \\
f_{\mathrm{nw}} = \int_0^{b/2} (\mathrm{d}f_{\mathrm{D}}.\alpha_r + \mathrm{d}f_{\mathrm{L}}).\mathrm{d}y \\
f_{\mathrm{tw}} = \int_0^{b/2} (\mathrm{d}f_{\mathrm{D}} + \mathrm{d}f_{\mathrm{L}}.\alpha_r).\mathrm{d}y \\
m_{\mathrm{x}} = \int_0^{\frac{b}{2}} y.(\mathrm{d}f_{\mathrm{D}}.\alpha_r + \mathrm{d}f_{\mathrm{L}}).\mathrm{d}y \\
m_{\mathrm{y}} = \int_0^{b/2} (x_{\mathrm{lr}} + y.\tan(\Lambda_{\mathrm{l}}) - c_{\mathrm{y}}/4).(\mathrm{d}f_{\mathrm{D}}.\alpha_r + \mathrm{d}f_{\mathrm{L}}).\mathrm{d}y \\
rp_{\mathrm{w}} = [m_{\mathrm{y}}/f_{\mathrm{nw}} \quad m_{\mathrm{x}}/f_{\mathrm{nw}} \quad 0]^{\mathrm{T}}
\end{gathered} \tag{7}
$$

y element of rp_w can be find by solving momentum around z axis due to f_{tw} too. f_{nw}, f_{tw} and rp_w elements are derived in (8).

$$f_{nw} = \rho c_r(C_L + C_D\alpha_r)\big((1+3\eta)b^3\dot{q}_1^4 + 24v_\infty^2(1+\eta)b\big)/192$$
$$f_{tw} = \rho c_r(C_L\alpha_r - C_D)\big((1+3\eta)b^3\dot{q}_1^4 + 24v_\infty^2(1+\eta)b\big)/192$$
$$\frac{m_x}{f_{nw}} = \frac{3(1+4\eta)b^3\dot{q}_1^4 + 40(1+\eta)v_\infty^2 b}{10(1+3\eta)b^2\dot{q}_1^4 + 240(1+\eta)v_\infty^2}$$
$$m_y/f_{nw} = ((3(1+4\eta)\tan(\Lambda_l)\,b - (6\eta^2+3\eta+1)c_r)b^2\dot{q}_1^4 + \cdots$$
$$\ldots 40(\eta+1)\tan(\Lambda_l)\,v_\infty^2 b - 40(\eta^2+\eta+1)v_\infty^2 c_r) \ldots$$
$$\ldots/(10b^2\dot{q}_1^4(1+3\eta) + 240v_\infty^2(1+\eta)) \qquad (8)$$

The virtual work of aerodynamic forces in term of generalized coordinates (Q_{aero}) can be derived as in (9). Here f_{aero} is aerodynamic force vector and rp is CoP position vector, both represented in base frame.

$$f_{aero} = R_x(q_1).[f_{tw} \quad 0 \quad -f_{nw}.\mathrm{sign}(\dot{q}_1)]$$
$$rp = R_x(q_1).rp_w$$
$$Q_{aero[4\times1]} = (\partial(rp(q))/\partial q)^T.f_{aero} \qquad (9)$$

T, d, d_{EOM}, Q_k and Q_{aero} are derived analytically using Maple software and not represented here. $\bar{M} = T^T M\, T^T$, d_{EOM} and (3) are evaluated numerically afterward to be integrated using a Runge-Kutta 4th order method.

E. Numerical Simulation

The assumptions and model parameters of the simulation are shown in table 1. Fig.s 2 and 3 show the joints angle and the absolute drag force vector for two consecutive flapping cycles (0.8 second). Aerodynamic force (f_{aero}) is symmetric with vertical component mean value near zero due to symmetric up-stroke and down-stroke motion. It shows the wing passively folds a little while it is flapping and wing tip follows an 8-shape path due to the membrane elasticity and links' inertia and weight (Fig. 4). A sequenced graph of the wing is shown in Fig. 4 too.

III. DESIGN AND IMPLEMENTATION

A. The Bat Wing Design and Implimention

Our wing skeleton is based upon previous research [13]. During the design phase, we opted to make a few adjustments to this specification, particularly with regards to the design of the joints. As our wing folding mechanism is not mechanically actuated, we were able to reduce the number of actuating mechanisms to one gearbox. This gearbox controls the upstroke and down-stroke of the wing only, the other wing movements are actuated via the elastic network of the wing. The completed design was 3D printed using ABS plastic. We created a network of 0.5mm elastic threads, similar to the layout of fibre bundles of a bat wing (Fig. 4) [1]. We then attached 0.25mm latex sheeting to this network using cyanoacrylate glue, and polyvinyl acetate glue as sealing. This elastic network serves as a structure for the wing membrane to attach on to. It allows the wing membrane to mimic the high stiffness strength along the digits of a live bat. We attached elastic across the wing so as to allow the elastic to maintain the constraints in (1). Our bat wing is powered by a modified Tamiya 70097 twin-motor gearbox using a 58:1 gear ratio. The gearbox was altered so that the output shafts operate in unison with each other. The bat wing is controlled with an Arduino Uno microcontroller board, using C++.

TABLE I. MODEL AND SIMULATION PARAMETERS

m_a	11e-3 [Kg]	x_{lr}	0.2× c_r [m]
m_f	19.8e-3 [Kg]	x_{lt}	0.5× c_t [m]
m_h	21e-3 [Kg]	l_0	5.0e-2 [m]
l_a	34e-3 [m]	k	2.7e1 [N/m]
l_f	62e-3 [m]	c_v	0.0 [Nm/s]
l_h	94e-3 [m]	α_a	3° [deg]
c_r	6.3e-3 [m]	C_{D0}	0.05
c_t	1.4e-3 [m]	e_w	1
ρ	1.2041 [Kg/m^3]	g	9.81 [m/s^2]
v_∞	5.0 [m/s]	l_{COM}	l_i / 2 (i: a, f, h) [m]
I_a (Arm inertia matrix)		diag[3.3, 0.017, 3.3]×1e-5 [Kg.m^2]	
I_f (Forearm int. matrix)		diag[6.2, 0.076, 6.3] ×1e-5 [Kg.m^2]	
I_h (Hand inertia matrix)		diag[1.0, 0.079, 1.1] ×1e-5 [Kg.m^2]	
Flapping parameters:		A = 70°, $\omega = 5\pi$, q_{1_0} = -10°	

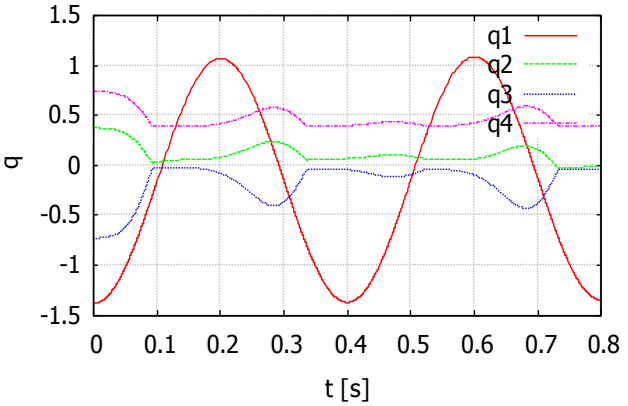

Fig. 2. Joint rotations for two flapping cycles. q_1 for the arm about the base frame x-axis and q_2, q_3 and q_4 are for the arm, elbow and wrist rotations about the local frame z-axes

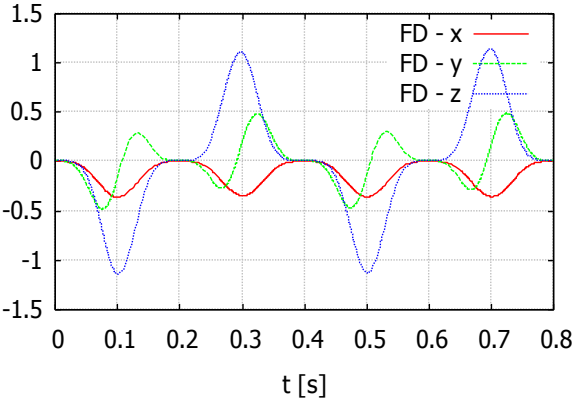

Fig. 3. Aerodynamic force components (f_{aero}) [N] for two consecutive flapping cycles.

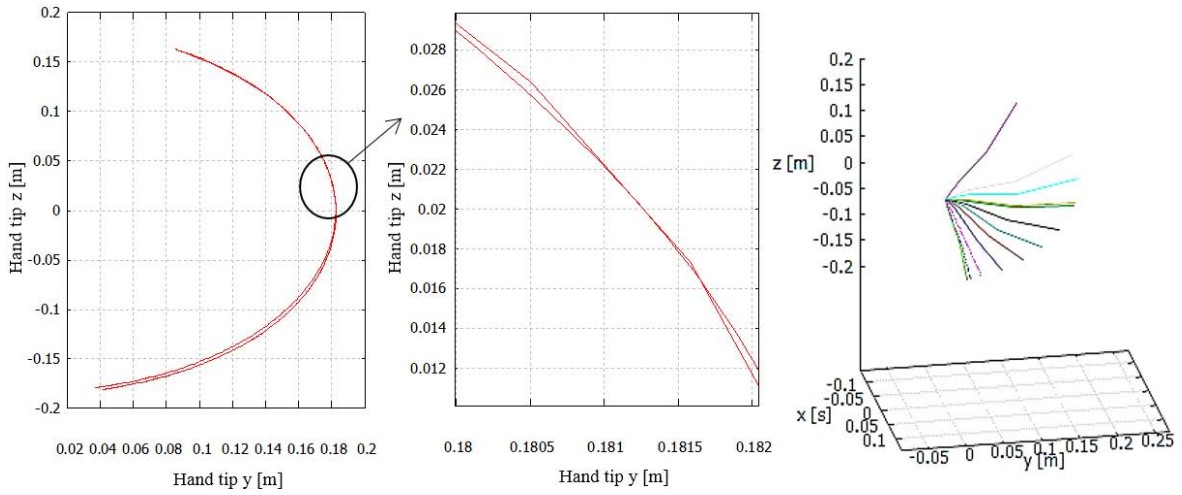

Fig. 4. 8-shape path of the hand tip projection on y-z plane for a full cycle (left). The intersection of the 8-shape path is maximized (middle). Sequential representation of small passive folding in upstroke in 3D space (right).

B. *Set-up Experiments Results*

We applied a low pass filter to the data and plotted a time series of both motors simultaneously (Fig. 5). We also plotted a return map for peaks in the data (Fig. 6). In order to observe how the limit cycle of the motor settles, the first half of the data for each motor is plotted in one colour (magenta and cyan), and the latter half in another (red and blue). We can see that the wing quickly settles down to a steady state. In order to observe the movement patterns of the wing, we attached an LED to the tip of the wing, and took 10 second long exposure photographs of the wing in motion at different speeds (Fig. 7). The wing extends upon the down-stroke, and folds mid-upstroke. One interesting observation is the extension that can be seen at the top of the upstroke, similar to the motion of a real bat. The wing will then extend during the down-stroke.

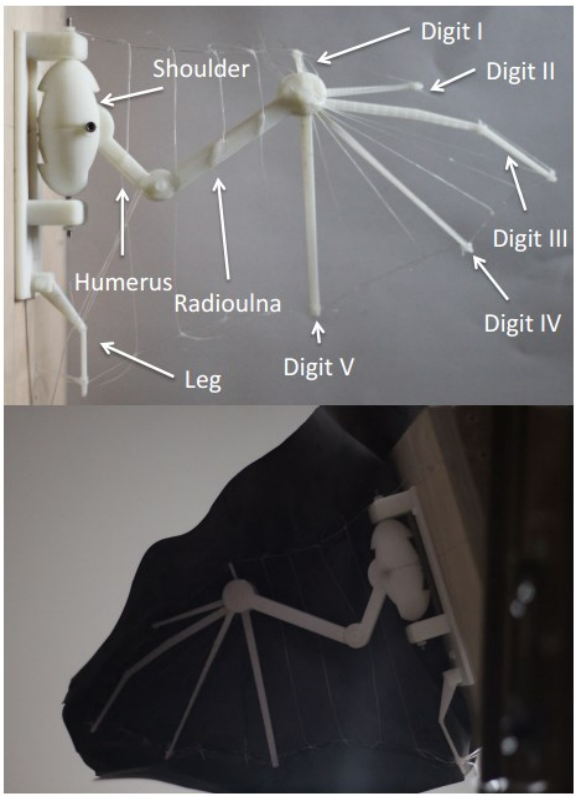

Fig. 5. Elastic network mimicking the layout of fibre bundles of a bat wing. Humerus: 37.2mm, Radioulna: 68.1mm, Digit I: 10.0mm, Digit II: Metacarpal 29.7mm, Proximal phalanx 6.9mm, Middle phalanx 4.1mm, Distal phalanx 2.6mm. Digit III: Metacarpal 39.9mm, Proximal phalanx 29.1mm, Distal phalanx 37.9. Digit IV: Metacarpal 42.61mm, Proximal phalanx 22.1mm, Distal phalanx 22.9mm. Leg: Femur 26.2mm, Tibia 31.5mm.

IV. Discussion

In this paper we focused on studying the role of anisotropic stiffness distribution in the bat wing membrane on the efficiency of upstroke. Biological literature suggest that the elastic membrane helps the bat to exploit passive collapsing of the wing at the end of the downstroke leading to reduced drag force during upstroke. Through numerical simulations and experiments we show that the anisotropy of the membrane contributes to such efficiency gains only at high speeds of flapping. We observed an eight-shaped passive elongation-collapsing steady state attractor at roughly 198 rpm speed of the motors. Though we expect the attractor to change shape with larger loop areas at higher speeds, we could not perform such experiments due to hardware limitations. Meanwhile, it proved difficult to simulate and construct a robotic wing that emulated the wing folding kinematics of a real bat using only one degree of actuated motion. Besides we can look at various wing alterations, possibly through computer simulation. For that means, a more precise dynamic model of the wing is needed that can profoundly show the characteristics of the wing membrane.

We showed that mimicking the behaviour of nature, such as the bat wing skin, can have practical and feasible applications in robotics. Further work could look into optimization of the structural design parameters to improve the passive folding mechanism in moderate and low flapping speed. Besides, different elastic networks can affect not only the timing and behaviour of wing folding in relation to a wing-beat, but also the flight properties of flapping wing UAVs. One such application could be the role of this elastic network in the UAV's ability to perform energy efficient quick and precise manoeuvres.

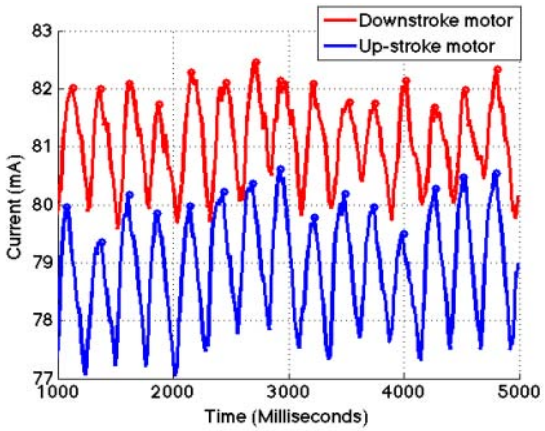

Fig. 6. Time series of current data after the application of a low pass filter for downstroke and up-stroke motors

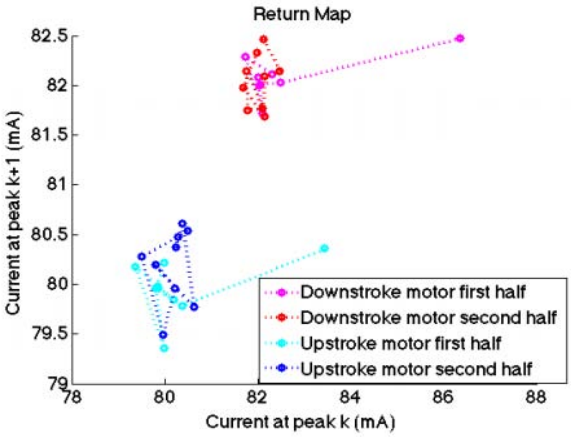

Fig. 7. Return map for peaks in the data for upstroke and downstroke motors, showing the steady state variability of the up-stroke and downstroke motor currents.

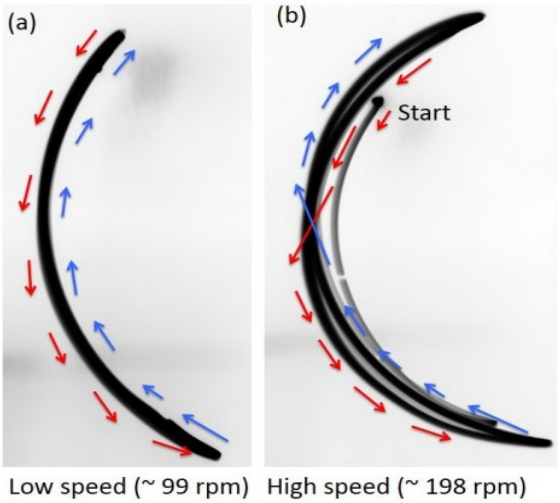

Fig. 8. Inverted black and white images depicting long exposures of robotic wing flapping at different speeds. a) Shows the wing flapping at a speed such that no wing extension and folding can be seen. b) shows the wing flapping at a speed high enough such that the wing passively extends and folds. The red arrows correspond to the downstroke, and the blue arrows correspond to the up-stroke.

V. Conclusion

We designed and built a robotic bat wing with an anisotropic membrane capable of performing the 8-shape wing-folding seen in bats' high speed flight passively. We can collect input power data from the wing, and observe wing-beat patterns. We conclude that the wing must maintain a minimum flapping frequency in order to exhibit its wing extending and folding behaviour effectively. The research potential of the anisotropic stiffness distribution of the bat wing and its practical applications is great. This robotic wing serves as a solid foundation for further exploration into the possibility and benefits of integrating this behaviour into flapping wing UAVs.

Acknowledgment

The authors would like to thank the UK Engineering and Physical Sciences Research Council (EPSRC) project REINS, grant no. EP/I028765/1, and the Seventh Framework Program of the European Commission in the framework of EU project STIFF-FLOP, grant agreement 287728.

References

[1] S. M. Swartz, M. S. Groves, H. D. Kim, and W. R. Walsh, "Mechancial properties of bat wing membrane skin," *J. Zool.*, vol. 239, no. 2, pp. 357–378, 1996.

[2] D. N. Beal, F. S. Hover, M. S. Triantafyllou, J. C. Liao, and G. V. Lauder, "Passive propulsion in vortex wakes," *J. Fluid Mech.*, vol. 549, no. 1, p. 385, Feb. 2006.

[3] X. Tian, J. Iriarte-Diaz, K. Middleton, R. Galvao, E. Israeli, A. Roemer, A. Sullivan, A. Song, S. Swartz, and K. Breuer, "Direct measurements of the kinematics and dynamics of bat flight," *Bioinspir. Biomim.*, vol. 1, no. 4, p. S10, 2006.

[4] S. S. Baek, K. Y. Ma, and R. S. Fearing, "Efficient resonant drive of flapping-wing robots," *intelligent Robot. Syst.*, pp. 2854–2860, 2009.

[5] M. A. Fenelon, "Biomimetic flapping wing aerial vehicle," *Robot. Biomimetics*, pp. 1053–1058, 2008.

[6] G. Bunget and S. Seelecke, "BATMAV: a biologically inspired micro air vehicle for flapping flight: kinematic modeling," In The 15th International Symposium on: Smart Structures and Materials & Nondestructive Evaluation and Health Monitoring, International Society for Optics and Photonics, pp. 69282F-69282F, 2008.

[7] P. D. Kuang, M. Dorothy, and S. Chung, "RoboBat : Dynamics and Control of a Robotic Bat Flapping Flying Testbed," in AIAA Infotech at Aerospace Conference, St. Louis, MO, pp. 2011-1435, 2011.

[8] J. Colorado, A. Barrientos, C. Rossi, J. W. Bahlman, and K. S. Breuer, "Corrigendum : Biomechanics of smart wings in a bat robot : morphing wings using SMA actuators," *Bioinspir. Biomim.*, vol. 3, no. 3, 2013.

[9] S. J. Furst, G. Bunget, and S. Seelecke, "Design and fabrication of a bat-inspired flapping-flight platform using shape memory alloy muscles and joints," *Smart Mater. Struct.*, vol. 22, no. 1, Jan. 2013.

[10] W. Shyy, H. Aono, S. K. Chimakurthi, P. Trizila, C.-K. Kang, C. E. S. Cesnik, and H. Liu, "Recent progress in flapping wing aerodynamics and aeroelasticity," *Prog. Aerosp. Sci.*, vol. 46, no. 7, pp. 284–327, Oct. 2010.

[11] B. Parslew, "Simulating Avian Wingbeats and Wakes," PhD diss, The University of Manchester, 2012.

[12] B. W. Tobalske, "Biomechanics of bird flight.," *J. Exp. Biol.*, vol. 210, no. Pt 18, pp. 3135–46, Sep. 2007.

[13] J. W. Bahlman, "Design and characterization of a multi-articulated robotic bat wing.," *Bioinspir. Biomim.*, vol. 8, no. 1, 2013.

[14] M. Wisse, R. Linde, and Q. van Der, *Delft Pneumatic Bipeds*, vol. 34. Springer Tracts in Advanced Robotics, Berlin Heidelberg, 2007.

[15] J. J. Bertin and R. C. M., Aerodynamics for Engineers, 5th ed. Prentice Hall, 2008.